Enhanced Uptake in a MOF@COF Composite by Interfacial Pore Generation

Luis Garzón-Tovar,[a],# Javier Pérez-Carvajal,[a],# Amirali Yazdi,[a] Jose Hernández-Muñoz,[b] Pedro Tarazona,[b] Inhar Imaz,*[a] Félix Zamora[c,d] and Daniel Maspoch*[a,e]

Abstract: Herein we describe a new class of porous composites comprising metal-organic framework (MOF) crystals confined in single spherical matrices made of packed covalent-organic framework (COF) nanocrystals. These MOF@COF composites are synthesized via a two-step method of spray-drying and subsequent amorphous (imine-based polymer)-to-crystalline (imine-based COF) transformation. This transformation around the MOF crystals generates micro- and mesopores at the MOF/COF interface that provide far superior porosity compared to the constituent MOF and COF components taken together. We report that water sorption in these new pores occurs within the same pressure window as in the COF pores. Our new MOF@COF composites, with their additional pores at the MOF/COF interface, should have implications for the development of new composites.

Combining different types of porous materials into composites can yield materials that, relative to their constituent components, exhibit greater porosity, new synergic properties, higher stability and novel shapes for myriad applications, including separation,[1] catalysis,[2] sensing,[3] pollutant removal[4] and gas capture.[5] Such composites tend to show hierarchical porosity. Most of them are formed by embedding one porous material into another one or by interfacing two porous materials.[6] Archetypal examples are mixed-matrix membranes (MMMs) in which a porous material (*e.g.* zeolite or metal-organic framework [MOF]) is incorporated into an amorphous porous polymeric film.[7]

Researchers have recently developed a class of crystalline porous polymers known as *covalent-organic frameworks* (COFs),[8] which enable use of COFs as components in porous composites. For example, Fu *et al.* recently developed a new class of membranes by interfacing a MOF ($Zn(bdc)_2(dabco)$ or ZIF-8) layer on top of a COF (COF-300) layer. The resulting membranes showed synergic enhancement of selective separation of H_2 over CO_2 relative to the summed separation capacity of the MOF and COF components.[9] Additionally, various groups have developed a series of core-shell MOF/COF composites that exhibit remarkable photocatalytic properties, mainly in H_2 evolution.[10]

Herein we present a new MOF@COF composite that we developed by confining MOF crystals in single spherical COF beads. In these beads, the MOF (UiO-66-NH_2 or Zr-fumarate) crystals are dispersed into a spherical matrix made of packed nanocrystals of COF-TAPB-BTCA, a two-dimensional COF assembled two trigonal building blocks: 1,3,5-benzenetricarbaldehyde (BTCA) and 1,3,5-tris-(4-aminophenyl)benzene (TAPB). Structurally, the beads are zero-dimensional versions of MOF-MMMs, in which the organic polymer matrix has been substituted with a crystalline COF matrix. Figure 1a shows the synthesis of these MOF/COF composite beads. First, spray-drying is used to encapsulate the MOF crystals into an amorphous, imine-based, TAPB-BTCA polymer bead. Then, the beads are subjected to dynamic covalent chemistry conditions, which transform the amorphous polymer into COF-TAPB-BTCA crystals.[11] We discovered that this amorphous-to-crystalline transformation around the MOF crystals generates pores at the MOF/COF interface, leading to a *ca.* three times higher N_2 BET surface area relative to the value expected from simply summing the respective contributions of each component (MOF and COF). In addition, we have proven that water adsorption in these pores occurs at the same P/P_0 as in the COF pores, which enables a three to four times increase of the water uptake step.

[a] Dr. Luis Garzón-Tovar, Dr. Javier Pérez-Carvajal, Dr. Amirali Yazdi, Dr. I. Imaz, Prof. D. Maspoch
Catalan Institute of Nanoscience and Nanotechnology (ICN2), CSIC and BIST
Campus UAB, Bellaterra, 08193 Barcelona, Spain
E-mail: inhar.imaz@icn2.cat, daniel.maspoch@icn2.cat
# Both authors contributed equally

[b] Jose Hernández-Muñoz, Prof. Pedro Tarazona
Departamento de Física Teórica de la Materia Condensada, IFIMAC Condensed Matter Physics Center, Universidad Autónoma de Madrid, Madrid, 28049, Spain

[c] Dr. Félix Zamora
Departamento de Química Inorgánica and Institute for Advanced Research in Chemical Sciences (IAdChem), Universidad Autónoma de Madrid, Madrid, 28049, Spain

[d] Dr. Félix Zamora
Instituto Madrileño de Estudios Avanzados en Nanociencia (IMDEA Nanociencia), Cantoblanco, 28049, Madrid, Spain

[e] Prof. D. Maspoch
ICREA
Pg. Lluís Companys 23, Barcelona, 08010, Spain

Supporting information for this article is given via a link at the end of the document

We began synthesis of the first composite by preparing **UiO-66-NH₂@COF-TAPB-BTCA** beads. A solution of BTCA (63 mg) in a mixture of DMSO and acetic acid (9 : 1 *v/v*, V_{total} = 15

SEM cross-sectional image of these **UiO-66-NH₂@COF-TAPB-BTCA** beads confirmed that the UiO-66-NH₂ particles were well dispersed within the COF matrix (Figure 1f). However, we
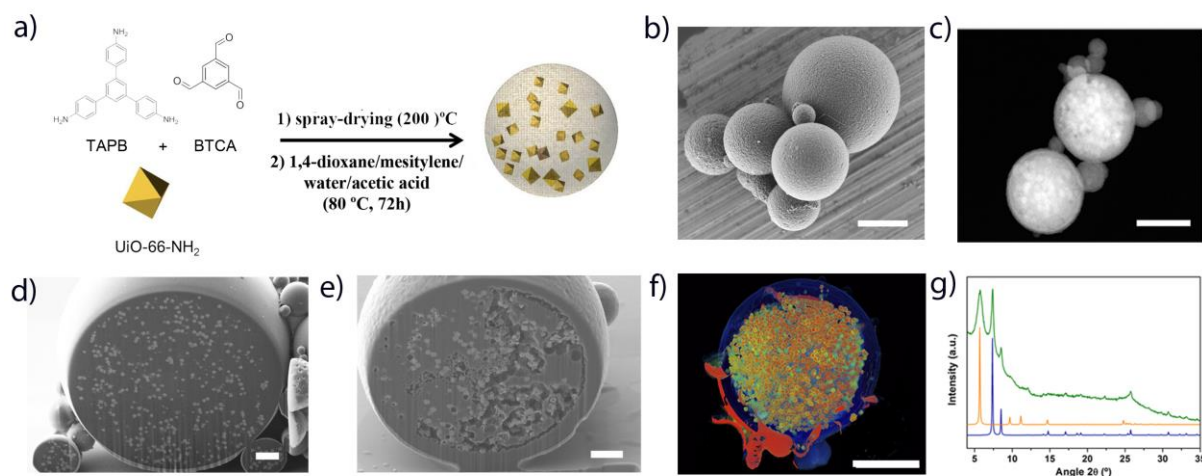

Figure 1 a) Schematic of the MOF@COF composite synthesis. b,c) Representative FESEM and HAADF-STEM images of microspherical **UiO-66-NH₂@COF-TAPB-BTCA** beads. d,e) FIB-SEM images of an imine-based polymeric bead containing encapsulated UiO-66-NH₂ crystals (d), and of a crystalline **UiO-66-NH₂@COF-TAPB-BTCA** bead (e). f) 3D reconstruction of a representative **UiO-66-NH₂@COF-TAPB-BTCA** bead. g) XRPD diffractogram for **UiO-66-NH₂@COF-TAPB-BTCA** (green), compared with the simulated powder patterns for UiO-66-NH₂ (blue) and COF-TAPB-BTCA (orange). Scale bars: b) 2.5 µm, c-e) 1 µm, and f) 3.5 µm.

mL) and a mixture of TAPB (143 mg) and UiO-66-NH₂ [40 mg; synthesized under solvothermal conditions; crystal size = 217 ± 32 nm; obtained as pure phase as confirmed by X-ray powder diffraction (XRPD), field-emission scanning electron microscopy (FE-SEM), N₂ sorption isotherm (S_{BET} = 1151 m²·g⁻¹; Supporting Information, Figures S1-S4)] in DMSO (15 mL) were independently atomized using a two-fluid nozzle (T-mode) at a feed rate of 3.0 mL min⁻¹, a flow rate of 336 mLmin⁻¹ and an inlet temperature of 200˚C, using a B-290 Mini Spray Dryer (BÜCHI Labortechnique). This atomization immediately afforded a yellow powder. High-angle annular dark-field scanning transmission electron microscopy (HAADF-STEM), FE-SEM and XRPD performed on this intermediate solid revealed the successful encapsulation of UiO-66-NH₂ crystals into amorphous spherical imine-based polymer beads (diameter: 0.5 µm to 10 µm; Supporting Information, Figures S5,S6). Additionally, focused ion beam scanning electron microscopy (FIB-SEM) cross-sectional images of these beads revealed a homogeneous distribution of UiO-66-NH₂ crystals within the dense, imine-based polymer matrix (Figure 1d). Nitrogen adsorption measurements performed at 77 K revealed that this intermediate solid was non-porous (Supporting Information, Figure S7), suggesting that the encapsulated MOF was not accessible to N₂ and confirming that the UiO-66-NH₂ had been incorporated into the polymer beads.

In the second synthetic step, we subjected the solid product from above to an amorphous-to-crystalline transformation by dispersing it into a mixture of 1,4-dioxane/mesitylene/water/acetic acid, and then heating under reflux the resulting dispersion at 80 ˚C for 72 h.[11] Remarkably, the XRPD pattern of the so-formed solid (hereafter, **UiO-66-NH₂@COF-TAPB-BTCA**) confirmed that the UiO-66-NH₂ had not been affected, and it showed a new diffraction peak at 5.5º, confirming the desired transformation into COF-TAPB-BTCA (Figure 1g). HAADF-STEM and FE-SEM images revealed confinement of UiO-66-NH₂ nanoparticles into beads created by the close packing of COF nanoparticles (Figures 1b,c). A FIB-

observed a COF shell, and a certain degree of hollowing of the dense matrix, during the COF crystallization (Figures 1d,e). We hypothesized that the COF shell formation and the hollowing that generated macroscale pores could have been due to inside-out Ostwald ripening, whereby COF crystallization on the surface of the sphere would be thermodynamically more favorable than inside the sphere, given the lower surface energy of surface crystals compared to internal ones.[12] Thus, we reasoned that formation of the shell by self-assembly of the COF crystals was due to the continuous dissolution of the core and subsequent migration to the shell. A similar phenomenon was observed by Banerjee *et al.* during formation of hollow spherical COFs. ENREF_5[13] In our composite beads, we estimated the content of Zr by digesting the powder (previously outgassed at 150 ºC) in a mixture of HNO₃/HF, and then analyzing it by inductively-coupled plasma optical-emission spectroscopy (ICP-OES). We found a UiO-66-NH₂ content of 15% wt%. The maximum achievable MOF loading in these COF-TAPB-BTCA beads was 15 wt%, as a higher quantity of UiO-66-NH₂ used in the synthesis precluded its complete encapsulation inside the beads. Note also that the optimum heating time for the amorphous-to-crystalline transformation was found to be 72 hours, as longer heating times resulted in etching of the UiO-66-NH₂ crystals (Supporting Information, Figure S8).

Once we had optimized the synthesis of **UiO-66-NH₂@COF-TAPB-BTCA**, we studied its N₂ adsorption properties (Figure 2a). We performed N₂ adsorption measurements at 77 K on the individual composite components (COF-TAPB-BTCA beads and UiO-66-NH₂; Supporting Information, Figures S3,S4,S12); a physical mixture of UiO-66-NH₂ and COF-TAPB-BTCA beads (15% and 85% w/w, respectively); and **UiO-66-NH₂@COF-TAPB-BTCA** beads (Figure 2a). As reported, UiO-66-NH₂ showed a type I isotherm, with a S_{BET} of 1151 m²·g⁻¹. The isotherms of the other three samples follow a complex type I trend, exhibiting a steep increase at low P/P₀ values, followed by a continuous and monotonic increase showing an H3 type hysteresis loop.[14] This
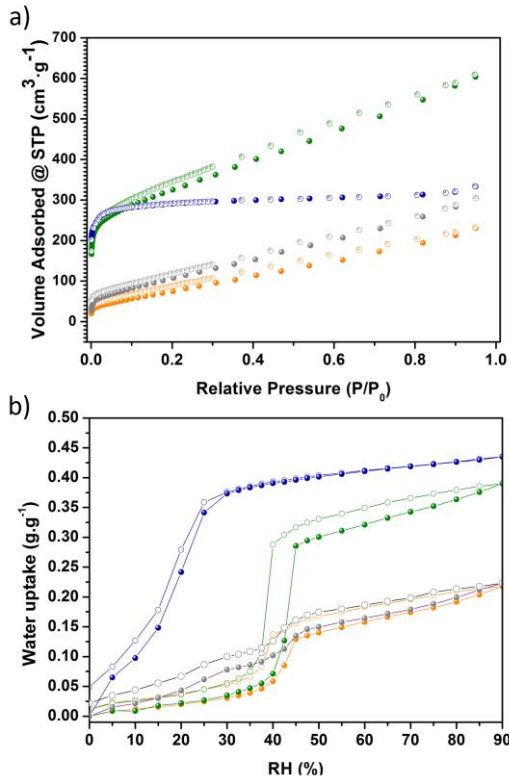
Figure 2. a) N$_2$ adsorption isotherms for UiO-66-NH$_2$ (blue), COF-TAPB-BTCA beads (orange), the physical mixture of these two components (grey) and **UiO-66-NH$_2$@COF-TAPB-BTCA** beads (green). b) Water adsorption isotherms for UiO-66-NH$_2$ (blue), COF-TAPB-BTCA beads (orange), the physical mixture of these two components (grey) and **UiO-66-NH$_2$@COF-TAPB-BTCA** (green).

complex trend with a non-distinctive plateau is common in microporous adsorbents comprising small agglomerated particles, which exhibit micropores and mesopores, and an external surface.[15] From these isotherms, we found S$_{BET}$ values of 319 m$^2 \cdot$g^{-1} for the COF-TAPB-BTCA beads, 420 m$^2 \cdot$g^{-1} for the physical mixture, and 1153 m$^2 \cdot$g^{-1} for the **UiO-66-NH$_2$@COF-TAPB-BTCA** (Supporting Information, Figures S10-S12). Note here that the S$_{BET}$ of the physical mixture was close to the expected value (445 m$^2 \cdot$g^{-1}) calculated by considering the isotherms for the COF-TAPB-BTCA beads and the UiO-66-NH$_2$ according to their respective mass proportions.

By comparing the four isotherms from above, we found that **UiO-66-NH$_2$@COF-TAPB-BTCA** beads exhibited a considerably higher S$_{BET}$ (1153 m$^2 \cdot$g^{-1}) than the summed S$_{BET}$ for the two components (420 m$^2 \cdot$g^{-1}). Given the similar structures of COF-TAPB-BTCA and **UiO-66-NH$_2$@COF-TAPB-BTCA** beads (*i.e.* a COF shell with internal hollowing), we attributed the higher surface area in the latter to the formation of pores of quasi-microscale (also known as *supermicropores*) in the interfaces between the MOF and COF crystals.[16] Formation of these pores was also reflected by the pore-size distribution (PSD; Supporting Information, Figure S13). The PSD of **UiO-66-NH$_2$@COF-TAPB-BTCA** showed the characteristic pore populations of both UiO-66-NH$_2$ (pore size: *ca.* 9 Å and 11 Å) and COF-TAPB-BTCA (pore size: *ca.* 17 Å) attributed to the intrinsic porosity of their frameworks. Additionally, we observed formation of a pore population ranging from *ca.* 18 Å to 32 Å in size, and a wider and larger population of pores (in comparison to COF-TAPB-BTCA) sized from 32 Å to beyond *ca.* 100 Å.

Having observed the formation of a hierarchical porous **UiO-66-NH$_2$@COF-TAPB-BTCA** composite, we then studied its water sorption properties. The collected water isotherm revealed an "S"-type sorption isotherm, exhibiting a main steep uptake between 0.35 P/P$_0$ and 0.50 P/P$_0$, and a maximum capacity

(q_{max}) of 0.39 g$\cdot$g^{-1} at 0.90 P/P$_0$ (Figure 2b). There are two interesting features in this isotherm. First, **UiO-66-NH$_2$@COF-TAPB-BTCA** beads also exhibited a much higher q_{max} at 0.90 P/P$_0$ than that expected from the mass contribution of both components (expected q_{max} = 0.25 g$\cdot$g^{-1}; measured q_{max} of the physical mixture = 0.22 g$\cdot$g^{-1}). This behavior resembles that observed for the higher N$_2$ uptake attributed to the enhanced porosity generated in the MOF/COF interface (*vide supra*). Secondly, the main steep water uptake in **UiO-66-NH$_2$@COF-TAPB-BTCA** beads occurred at the same P/P$_0$ range than in the pure COF-TAPB-BTCA beads and in the physical mixture. Moreover, this steep water uptake is more than three times (0.26 g$\cdot$g^{-1}) that of the physical mixture (0.07 g$\cdot$g^{-1}) and nearly three times that of the COF-TAPB-BTCA beads (0.09 g$\cdot$g^{-1}).

Based on the above observations, we hypothesized that the COF pores, and the pores generated at the MOF/COF interface, rapidly fill with water molecules within the same pressure window. To corroborate our hypothesis, we performed a theoretical calculation of water molecules filling the pores, using a Landau-Ginzburg density functional representation of water, and a simple geometrical model for the hierarchical structure of interfacial pores between COF-like and MOF-like walls. The thermodynamic condition for the filling of a pore of radius r is $P/P_o \cong 1 - w \cos(\theta)/r$, where θ is the contact angle of the liquid on the walls, and the length $w \equiv 2\gamma/(RT\,\rho_{liq})$ is $\approx 1\,nm$ with the surface tension, γ, and the molar density of water. Interfacial (irregular) pores would be represented by a broad distribution of effective values for r, which would gradually fill at increasing vapor pressure, at a rate depending on $\cos(\theta)$, thus describing the mean hydrophilicity of the confining COF walls. At $P = P_{COF}$, the nanopores of COF-TAPB-BTCA fill and there is a sudden jump $\Delta\langle\cos(\theta)\rangle_{ef} \approx a_p$, in the effective contact angle of water on these surfaces, where $a_p \approx 0.07$ is the ratio of the nanopore normal section across the COF-TAPB-BTCA crystal. All the interfacial spaces within a width $\Delta r \approx a_p w/(1 - P_{COF}/P_o)$, for their effective radii, would be filled at the same humidity as the COF pores. We employed this approach to extract a smooth distribution of (effective) size for the interfacial pores from the experimental adsorption curves.

As a proof-of-principle for the validity of the mesoscopic thermodynamic analysis, we explored the effect at molecular scale, through a Landau-Ginzburg Density Functional analysis of the grand potential energy

$$\Omega[\rho] = \int dr \left(f(\rho(r)) + \frac{b}{2}\left(\nabla\rho(r)\right)^2 + (V(r) - \mu)\,\rho(r) \right),$$

in terms of the bulk free energy density of a Lennard-Jones fluid and a square gradient term, with parameters to reproduce the phase coexistence and surface tension of water, in a confining external potential $V(r)$ with the geometrical structure of cavities confined between porous walls. The results confirm that all the interfacial pores, within a range of sizes (in our calculations: from 26 Å to 34 Å), are collectively filled at the same pressure at which the regular pores of the COF-like wall are filled (Supporting Information, Section 4). The theoretical analysis fully corroborates a generic concept important for increasing the sorption uptake step of adsorbents for water-sorption applications, including water harvesting, humidity control, and adsorption heat pumps and chillers.

To demonstrate the generality of our approach, we synthesized a second composite under similar conditions, substituting UiO-66-NH$_2$ with Zr-fumarate [synthesized under solvothermal conditions; crystal size = 20 ± 12 nm; obtained as pure phase as confirmed by XRPD, HAADF-STEM and N$_2$
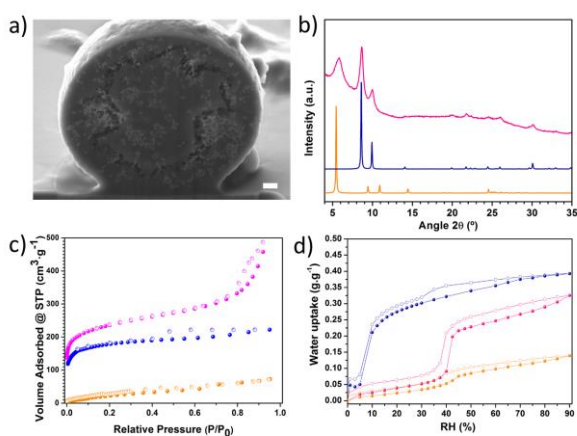
Figure 3. a) FIB-SEM images of **Zr-fumarate@COF-TAPB-BTCA** beads. Scale bar = 200 nm. b) XRPD diffractogram for **Zr-fumarate@COF-TAPB-BTCA** (pink), compared with the simulated powder patterns for Zr-fumarate (blue) and COF-TAPB-BTCA (orange). c) N_2 adsorption isotherms for Zr-fumarate (blue), COF-TAPB-BTCA beads (orange) and **Zr-fumarate@COF-TAPB-BTCA** beads (pink). d) Water sorption isotherms for Zr-fumarate (blue), COF-TAPB-BTCA (orange) and **Zr-fumarate@COF-TAPB-BTCA** (pink).

sorption isotherm (S_{BET} = 830 $m^2 \cdot g^{-1}$; Supporting Information, Figures S20-22]. After the two-step synthesis, FIB-SEM cross-sectional and HAADF-STEM images, and XRPD, of the resulting solid revealed formation of crystalline beads of COF-TAPB-BTCA in which the Zr-fumarate particles were encapsulated (Figure 3a,b; Supporting Information, Figure S20). In this case, the optimum heating time for the amorphous to crystalline transformation process was determined to be 18 hours; again, further heating caused etching of the Zr-fumarate crystals. As for UiO-66-NH$_2$ content in the first composite, the Zr-fumarate content in **Zr-fumarate@COF-TAPB-BTCA** was estimated by ICP-OES, and a value of 18% wt% was found.

Similarly to the UiO-66-NH$_2$ composite, the N_2 and the H$_2$O adsorption isotherms of **Zr-fumarate@COF-TAPB-BTCA** beads both showed *ca.* three-fold higher S_{BET} (700 $m^2 \cdot g^{-1}$) and *ca.* two-fold higher q_{max} (0.32 $g \cdot g^{-1}$) values relative to those expected from the collective contribution of the two components (Figure 3c,d; Supporting Information, Figures S22-S24). Thus, the expected S_{BET} value was calculated to be 240 $m^2 \cdot g^{-1}$ and the expected q_{max} value, 0.19 $g \cdot g^{-1}$, based on the mass proportion of each component: 18 wt% of pristine Zr-fumarate nanoparticles (S_{BET} = 830 $m^2 \cdot g^{-1}$; q_{max} = 0.39 $g \cdot g^{-1}$) and 82 *wt%* of COF-TAPB-BTCA beads (S_{BET} = 110 $m^2 \cdot g^{-1}$; q_{max} = 0.14 $g \cdot g^{-1}$; heated for 18 hours). Likewise, the water isotherm revealed an "S"-type sorption isotherm exhibiting a steep uptake between 0.35 P/P$_0$ and 0.50 P/P$_0$ *ca.* four-fold (0.17 $g \cdot g^{-1}$) that expected from the mass contribution of COF-TAPB-BTCA beads (0.04 $g \cdot g^{-1}$). Together, our results confirmed the formation of additional pores at the MOF/COF interfaces.

In conclusion, we have synthesized microspherical MOF/COF composite beads by encapsulating MOF crystals within a crystalline COF matrix, through a two-step process of spray-drying and dynamic covalent chemistry. We have shown that pores are generated at the MOF/COF interface and that these pores provide a synergic increase in both N_2 and H$_2$O uptake relative to the constituent components. The N_2 sorption increase occurs within the low-pressure regime, whereas the higher H$_2$O uptake occurs within the pressure zone of steep adsorption increase characteristic of the pure COF-TAPB-BTCA beads. These two observations suggest that the sizes of the newly formed pores are within the supermicropore regime and that they are similar to the COF pores. We expect that the ability to generate additional pores at MOF/COF interfaces should have implications in the development of new composite materials: for example, for water-sorption applications and especially, in the fabrication of composite membranes.

Conflict of interest

The authors declare no conflict of interest.

[1]   T. Rodenas, I. Luz, G. Prieto, B. Seoane, H. Miro, A. Corma, F. Kapteijn, F. X. Llabrés i Xamena, J. Gascon, *Nat. Mater.* **2014**, *14*, 48.

[2]   H.-W. Liang, X. Zhuang, S. Brüller, X. Feng, K. Müllen, *Nat. Comm.* **2014**, *5*, 4973.

[3]   M. Tubaishat, S. Madria, *IEEE Potentials* **2003**, *22*, 20-23.

[4]   B. Hudaib, V. Gomes, J. Shi, C. Zhou, Z. Liu, *Sep. Purif. Technol.* **2018**, *190*, 143-155.

[5]   D. Qian, C. Lei, G.-P. Hao, W.-C. Li, A.-H. Lu, *ACS Appl. Mater. Interfaces* **2012**, *4*, 6125-6132.

[6]   a) X.-Y. Yang, L.-H. Chen, Y. Li, J. C. Rooke, C. Sanchez, B.-L. Su, *Chem. Soc. Rev.* **2017**, *46*, 481-558; b) B. R. Thompson, T. S. Horozov, S. D. Stoyanov, V. N. Paunov, *J. Mater. Chem. A* **2019**; c) J. Zhou, B. Wang, *Chem. Soc. Rev.* **2017**, *46*, 6927-6945; d) C. Triantafillidis, M. S. Elsaesser, N. Hüsing, *Chem. Soc. Rev.* **2013**, *42*, 3833-3846; e.M.-H. Sun, S.-Z. Huang, L.-H. Chen, Y. Li, X.-Y. Yang, Z.-Y. Yuan, B.-L. Su, *Chem. Soc. Rev.* **2016**, *45*, 3479-3563.

[7]   a) B. Zornoza, C. Tellez, J. Coronas, J. Gascon, F. Kapteijn, *Microp. Mesoporous Mater.* **2013**, *166*, 67-78; b) Y. Cheng, Y. Ying, S. Japip, S.-D. Jiang, T.-S. Chung, S. Zhang, D. Zhao, *Adv. Mater.* **2018**, *30*, 1802401; c) T. Ma, E. A. Kapustin, S. X. Yin, L. Liang, Z. Zhou, J. Niu, L.-H. Li, Y. Wang, J. Su, J. Li, X. Wang, W. D. Wang, W. Wang, J. Sun, O. M. Yaghi, *Science* **2018**, *361*, 48-52.

[8]   a) A. P. Côté, A. I. Benin, N. W. Ockwig, M. O'Keeffe, A. J. Matzger, O. M. Yaghi, *Science* **2005**, *310*, 1166-1170; b) B. J. Smith, L. R. Parent, A. C. Overholts, P. A. Beaucage, R. P. Bisbey, A. D. Chavez, N. Hwang, C. Park, A. M. Evans, N. C. Gianneschi, W. R. Dichtel, *ACS Cent. Sci.* **2017**, *3*, 58-65.

[9]   J. Fu, S. Das, G. Xing, T. Ben, V. Valtchev, S. Qiu, *J. Am. Chem. Soc* **2016**, *138*, 7673-7680.

[10]   a) D. Sun, S. Jang, S.-J. Yim, L. Ye, D.-P. Kim, *Adv. Funct. Mater.* **2018**, *28*, 1707110; b) Y. Peng, M. Zhao, B. Chen, Z. Zhang, Y. Huang, F. Dai, Z. Lai, X. Cui, C. Tan, H. Zhang, *Adv. Mater.* **2018**, *30*, 1705454; c) F.-M. Zhang, J.-L. Sheng, Z.-D. Yang, X.-J. Sun, H.-L. Tang, M. Lu, H. Dong, F.-C. Shen, J. Liu, Y.-Q. Lan, *Angew. Chem.* **2018**, *130*, 12282-12286; d) F. Li, D. Wang, Q.-J. Xing, G. Zhou, S.-S. Liu, Y. Li, L.-L. Zheng, P. Ye, J.-P. Zou, *Appl. Catal., B.* **2019**, *243*, 621-628.

[11]   a) L. Garzon-Tovar, C. Avci-Camur, D. Rodriguez-San-Miguel, I. Imaz, F. Zamora, D. Maspoch, *Chem. Commun.* **2017**, *53*, 11372-11375; b) B. J. Smith, N. Hwang, A. D. Chavez, J. L. Novotney, W. R. Dichtel, *Chem. Commun.* **2015**, *51*, 7532-7535.

[12]   Z. Wang, L. Zhou, X. W. Lou, *Adv. Mater.* **2012**, *24*, 1903-1911.

[13]   S. Kandambeth, V. Venkatesh, D. B. Shinde, S. Kumari, A. Halder, S. Verma, R. Banerjee, *Nat. Commun.* **2015**, *6*, 6786.

[14]   K. S. W. Sing, F. Rouquerol, J. Rouquerol, P. Llewellyn, in *Adsorption by Powders and Porous Solids (Second Edition)* (Eds.: F. Rouquerol, J. Rouquerol, K. S. W. Sing, P. Llewellyn, G. Maurin), Academic Press, Oxford, **2014**, pp. 269-302.

[15]   K. S. W. Sing, F. Rouquerol, P. Llewellyn, J. Rouquerol, in *Adsorption by Powders and Porous Solids (Second Edition)* (Eds.: F. Rouquerol, J. Rouquerol, K. S. W. Sing, P. Llewellyn, G. Maurin), Academic Press, Oxford, **2014**, pp. 303-320.

[16]   a) R. Semino, J. C. Moreton, N. A. Ramsahye, S. M. Cohen, G. Maurin, *Chem. Sci.* **2018**, *9*, 315-324; b) Y. Cheng, Y. Ying, L. Zhai, G. Liu, J. Dong, Y. Wang, M. P. Christopher, S. Long, Y. Wang, D. Zhao, *J. Memb. Sci.* **2019**, *573*, 97-106.

Entry for the Table of Contents (Please choose one layout)

Layout 1:

COMMUNICATION

A new class of porous composites comprising metal-organic framework (MOF) crystals confined in single spherical matrices made of packed covalent-organic framework (COF) nanocrystals is described. These MOF@COF composites show the formation of micro- and mesopores at the MOF/COF interface that provide superior porosity compared to the constituent MOF and COF components taken together.

MOF@COF Composite Beads

COF

MOF/COF interfacial pores

MOF
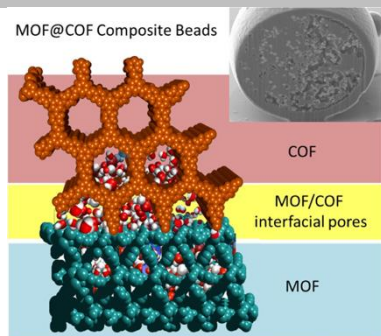
Luis Garzón-Tovar, Javier Pérez-Carvajal, Amirali Yazdi, Jose Hernández-Muñoz, Pedro Tarazona, Inhar Imaz,[*] Félix Zamora and Daniel Maspoch[*]

Page No. – Page No.

Enhanced Uptake in a MOF@COF Composite by Interfacial Pore Generation